Title
A high-resolution photon-counting breast CT system with tensor-framelet based iterative image reconstruction for radiation dose reduction

Journal
Physics in Medicine and Biology, 59(20)

ISSN
0031-9155

Authors
Ding, Huanjun
Gao, Hao
Zhao, Bo
et al.

Publication Date
2014-10-21

DOI
10.1088/0031-9155/59/20/6005

HHS Public Access

Author manuscript

Phys Med Biol. Author manuscript; available in PMC 2017 January 08.

Published in final edited form as:

Phys Med Biol. 2014 October 21; 59(20): 6005–6017. doi:10.1088/0031-9155/59/20/6005.

A high-resolution photon-counting breast CT system with tensor-framelet based iterative image reconstruction for radiation dose reduction

Huanjun Ding[1], **Hao Gao**[2], **Bo Zhao**[1], **Hyo-Min Cho**[1], and **Sabee Molloi**[1]

[1]Department of Radiological Sciences, University of California, Irvine, CA 92697

[2]Schoolof Biomedical Engineering and Department of Mathematics, Shanghai Jiao Tong University, Shanghai, 200240, People's Republic of China

Abstract

Both computer simulations and experimental phantom studies were carried out to investigate the radiation dose reduction with tensor framelet based iterative image reconstruction (TFIR) for a dedicated high-resolution spectral breast computed tomography (CT) based on a silicon strip photon-counting detector. The simulation was performed with a 10 cm-diameter water phantom including three contrast materials (polyethylene, 8 mg/ml iodine and B-100 bone-equivalent plastic). In the experimental study, the data were acquired with a 1.3 cm-diameter polymethylmethacrylate (PMMA) phantom containing iodine in three concentrations (8, 16 and 32 mg/ml) at various radiation doses (1.2, 2.4 and 3.6 mGy) and then CT images were reconstructed using filtered-back-projection (FBP) technique and TFIR technique, respectively. The image quality between these two techniques was evaluated by the quantitative analysis on contrast-to-noise ratio (CNR) and spatial resolution that was evaluated using the tasked-based modulation transfer function (MTF). Both simulation and experimental results indicated that the task-based MTF obtained from TFIR reconstruction with one-third of the radiation dose was comparable to that from FBP reconstruction for low contrast target. For high contrast target, TFIR was substantially superior to FBP reconstruction in term of spatial resolution. In addition, TFIR was able to achieve a factor of 1.6 to 1.8 increase in CNR depending on the target contrast level. This study demonstrates that TFIR can reduce the required radiation dose by a factor of two-third for a CT image reconstruction compared to FBP technique. It achieves much better CNR and spatial resolution for high contrast target in addition to retaining similar spatial resolution for low contrast target. This TFIR technique has been implemented with a graphic processing unit (GPU) system and it takes approximately 10 seconds to reconstruct a single-slice CT image, which can be potentially used in a future multi-slit multi-slice (MSMS) spiral CT system.

Keywords

Tensor framelet; Modulation transfer function; Contrast-to-noise ratio; Spatial resolution; High-resolution

Corresponding Author and Reprint Address: Sabee Molloi, PhD, Department of Radiological Sciences, Medical Sciences I, B-140, University of California, Irvine, CA 92697, Telephone: (949) 824-5904, symolloi@uci.edu.

1. Introduction

The radiation dose in computed tomography (CT) is a matter of important societal concern. It is always expected that a CT scan is completed with as low as possible radiation dose, while the CT image quality is maintained. Many efforts have been made for this purpose, including developing new detector technologies and investigating new image reconstruction techniques.

In recent years, energy-resolving photon-counting detectors have been investigated to achieve higher quality images with lower radiation dose compared to charge-integrating detectors. The state-of-art photon-counting detectors are generally based on direct conversion semiconductors. Cadmium-Zinc-Telluride (CZT) is one of the widely used crystals and has been investigated intensively for its several advantages over traditional detectors, such as high quantum detection efficiency as a result of its large effective atomic number (49.6), high mass density (5.8 g/cm^3) and excellent energy resolution (Bert *et al.*, 2003; Chmeissani *et al.*, 2004; Bisogni *et al.*, 2007; Shikhaliev, 2008; Wang *et al.*, 2010; Taguchi *et al.*, 2009; Barber *et al.*, 2009; Shikhaliev and Fritz, 2011; Le *et al.*, 2010). However, CZT detectors suffer from its low charge carrier mobility which leads to pulse pileup from high-count rate x-ray sources. Therefore, silicon strip is selected to build a photon-counting detector for its advantages in high charge carrier mobility and the lack of fluorescence in detectability range (Beuville *et al.*, 1998; Bert *et al.*, 2003; Frallicciardi *et al.*, 2009). The quantum efficiency of silicon-strip detectors declines as the tube voltage increases due to its relatively low atomic number. However, good detector efficiency can be obtained if edge-on illumination is used, which effectively increases the attenuation length to achieve a higher quantum detection efficiency (Bornefalk and Danielsson, 2010). A high-resolution silicon-strip detector utilizing this edge-on technology with a pixel pitch of 100 μm was used in this study.

In addition to the development of detector technologies, the technique of CT image reconstruction has also been investigated in order to reduce the radiation dose. The traditional method to reconstruct CT images is filtered-back-projection (FBP) because it is computationally fast, accurate and easily implemented (Herman, 1980; Kak and Slaney, 1988). However, FBP generally needs a large number of projections for the CT image reconstruction because projections must be discretized at a high sampling rate for the image quality to be satisfactory. To reduce the radiation dose, new algorithms are desirable to reconstruct images without any loss in image quality. In fact, a number of algorithms have been developed, such as Algebraic Reconstruction Techniques (ART) in 1970 (Gordon *et al.*, 1970) and Simultaneous Algebraic Reconstruction Techniques (SART) in 1984 (Anderson and Kak, 1984). These algorithms assume that projections through the object are modeled by a linear system of equations based on the discretization of the Radon transform and then are solved iteratively. However, these techniques were overlooked due to their performance requirements in the past and had been rediscovered recently for the image reconstruction of low-dose CT because of the dramatic development of high-performance computing techniques over the past decades (Elbakri and Fessler, 2002; Bian *et al.*, 2012; Casteele *et al.*, 2012; Hernandez *et al.*, 2012; Makeeva *et al.*, 2012; Pachon *et al.*, 2012). There has been several iterative reconstruction mechanisms developed for specific purposes, such as total

variation (TV) minimization, dictionary learning and tensor framelet. TV assumes that the image gradient is sparse and minimizes the total variation of the estimated images, and has been used for low-dose, few-view, limited-angle, and truncated data CT (Donoho, 2006; Sidky *et al.*, 2006; Yu and Wang, 2009). However, it may reduce the diagnostic values of reconstructed images due to undesirable biases and artifacts as well as loss of fine features. Dictionary learning usually learns from a set of given high-quality samples and then processes the image patch by patch to naturally and adaptively impose the strong structural constraints, which is more effective in terms of a sparse representation (Xu *et al.*, 2012). It has the disadvantage of acquiring accurate sample images to build dictionaries, and is not effective for a totally unknown object. Tensor framelet based iterative image reconstruction (TFIR) has been previously proposed (Gao *et al.*, 2012); (Gao *et al.*, 2013) to address the piecewise-constant artifacts by TV, through a multi-level and multi-filtered tensor version of tight frame. TFIR offers a general sparse representation and total variation with high-order differencing, and it also generalizes the wavelet with redundant representation (Gao *et al.*, 2012). Its flexibility and usefulness renders it as a natural choice for our study.

Our previous studies (Zhao *et al.*, 2012; Zhao *et al.*, 2013) comparing TFIR with FBP using postmortem breasts showed promising contrast-to-noise ratio (CNR) improvement at a low radiation dose. However, it remains to be seen if a similar dose reduction can be expected for a high-resolution breast CT system, in order to confirm that the CNR improvement from TFIR was not achieved by sacrificing the spatial resolution of the reconstructed images. In addition, recent studies indicate that spatial resolution depends on both the radiation dose and contrast targets for iterative reconstruction techniques (Richard *et al.*, 2012; Wilson *et al.*, 2013). Therefore, it is important to evaluate the performance of TFIR technique for a high-resolution detector by using various contrast targets and radiation doses. In this context, the tasked-based modulation transfer function (MTF), which can be measured with specific phantom designs, can be used for the comparison of spatial resolution between FBP and TFIR techniques (Richard *et al.*, 2012; Wilson *et al.*, 2013).

In this study, we utilize both developments in the detector technology and the image reconstruction technique to investigate the feasibility of radiation dose reduction by implementing a TFIR technique in a spectral breast CT system using a high-resolution photon-counting detector based on a silicon strip. The benefits of using photon-counting detectors, in comparison with conventional charge-integrating detectors, have been previously reported (Le *et al.*, 2010). This study focuses on quantitative comparisons of FBP and TFIR techniques for various contrast and spatial resolutions. In section II, we introduce the TFIR technique, the dedicated high-resolution breast CT system, image acquisition and quantitative analysis. In section III, we report our simulation and experimental results by comparing spatial resolution using tasked-based MTF and CNR between FBP and TFIR techniques with various radiation doses. In section IV, we discuss relevant issues and the possible application of the TFIR technique for a new breast CT system.

2. Methods and materials

2.1. The TFIR technique

The image reconstruction technique used in this study is based on the tensor-framelet (TF), denoted by W in the following formula (Gao *et al.*, 2012); (Gao *et al.*, 2013):

$$X=\arg\min_{X}\frac{1}{2}\|AX-Y\|_2^2+\lambda\|WX\|_1. \quad (1)$$

In equation (1), A is the system matrix corresponding to the X-ray transform of the breast CT system, a discretized Radon transform in 2D(Gao, 2012), X is the image to be reconstructed, Y is the acquired data after the log transform, and λ balances the data fidelity and the sparsity regularization.

Considering a one-level TF, the averaging operator is defined as

$$D_0X\big|_{ijk}=\begin{bmatrix} D_{0x}X \\ D_{0y}X \\ D_{0z}X \end{bmatrix}\Big|_{ijk}=\frac{1}{4}\begin{bmatrix} X_{i+1,j,k}+2X_{ijk}+X_{i-1,j,k} \\ X_{i,j+1,k}+2X_{ijk}+X_{i,j-1,k} \\ X_{i,j,k+1}+2X_{ijk}+X_{i,j,k-1} \end{bmatrix}, \quad (2)$$

Then the derived TF transform is

$$WX=\frac{1}{\sqrt{3}}\begin{bmatrix} D_0X \\ D_1X \\ D_2X \end{bmatrix}, \quad (3)$$

and the TF norm is defined as

$$\|WX\|_1=\frac{1}{\sqrt{3}}(\lambda_0\|D_0X\|_1+\lambda_1\|D_1X\|_1+\lambda_2\|D_2X\|_1) \quad (4)$$

where $W^TW=I$.

With TF, the Split Bregman method (Goldstein and Osher, 2009) is chosen to solve the convex L1-type problem in equation (1). Different to other algorithms, such as the quadratic penalty method (Jorge and Stephen, 1999), which implement a varying regularization parameter instead of the Bregman term and reduce the parameter λ dynamically during iterations to optimize image quality, the Split Bregman method works with a fixed and sufficiently large λ. An auxiliary variable d is introduced with $d=WX$, which is then transformed into the following unconstrained problem through the L2 penalty of the equality constraint,

$$X=\arg\min_X \frac{1}{2}\|AX-Y\|_2^2+\lambda\|d\|_1+\frac{\mu}{2}\|WX-d\|_2^2. \quad (5)$$

Instead of dynamically reducing μ, we use the same Bregman strategy with a fixed μ and another auxiliary variable v, and the iterations are

$$\begin{aligned} X^{n+1}&=\arg\min_X \|AX-Y+f^n\|_2^2+\mu\|WX-d^n+v^n\|_2^2 \\ f^{n+1}&=f^n+AX^{n+1}-Y \\ d^{n+1}&=\arg\min_d \tfrac{1}{2}\|d-(WX^{n+1}+v^n)\|_2^2+\tfrac{\lambda}{\mu}\|d\|_1 \\ v^{n+1}&=v^n+WX^{n+1}-d^{n+1} \end{aligned} \quad (6)$$

Note that the first step (L2 minimization step) of equation (6) is differentiable and therefore can be solved via

$$(A^TA+\mu)X^{n+1}=A^T(Y-f^n)+\mu W^T(d^n-v^n), \quad (7)$$

with the TF property $W^TW=I$. This equation can be conveniently solved by conjugated gradient method with point-wise operations instead of forming the matrix.

To summarize, our solution algorithm for solving equation (5) is through the following simple-to-implement Bregman loop with $X^n=d^n=v^n=f^n=0$

$$\begin{aligned} (A^TA+\mu)X^{n+1}&=A^T(Y-f^n)+\mu W^T(d^n-v^n) \\ f^{n+1}&=f^n+AX^{n+1}-Y \\ d^{n+1}&=S(WX^{n+1}+v^n,\lambda/\mu) \\ v^{n+1}&=v^n+WX^{n+1}-d^{n+1} \end{aligned} \quad (8)$$

Regarding the stopping criterion for the image reconstruction with the experimental data, we define

$$\varepsilon^n=\|X^n-X^{n-1}\|_1/\|X^n\|_1 \quad (9)$$

and find the following to be a robust stopping criterion

$$(\#(\varepsilon^{n+1}<\varepsilon^n)\geq\varepsilon_1)\|(\#(\varepsilon^{n+1}<\varepsilon^n<\varepsilon^{n-1})\geq\varepsilon_2). \quad (10)$$

where "#" denotes the number of appearance. Here we choose $\varepsilon_1=3$ and $\varepsilon_2=1$. Then the iteration stops when the non-decreasing residual consecutively happens three times or the non-decreasing twice-in-a-row residual happens once.

2.2. Breast CT with silicon strip photon-counting detector

A bench-top breast CT system was constructed for this study consisting of an x-ray tube (Spellman X4009), fore and after collimators, rotation and translation stage platform and silicon strip detector (see figure 1). The fore and after collimators consist of 3 mm thick lead sheets with 0.3 and 0.5 mm slit width and attached to the exit window of the tungsten target x-ray tube and the entrance window of silicon strip detector, respectively. The rotation and translation stage platform is built on a high precision direct drive rotary (DDR) motor (Kollmorgen Goldline DDR D062M, Danaher Motion, Wood Dale, IL) to provide both vertical and horizontal translations and extend the field of view beyond the size limitation of the detector. The distance between the source and isocenter is approximately 0.9 5 m.

To maximize the field of view, silicon strip photon-counting detector (DxRay Inc., Northridge, CA) is placed 1.05 m from the x-ray tube. The detector consists of a single line of 256 pixels with a pixel pitch of 100 μm, leading to a total length of 25.6 mm. The Si wafer is edge illuminated with a 5° tilt to increase the effective attenuation path to approximately 6 mm. The detector design specifications contain all the features required for the purpose of high resolution (spatial and energy): a 32-channel fast application specific integrated circuits (ASIC) readout (1×10^6 cps per pixel) with an extremely low noise level (< 4 keV) and an excellent energy resolution (< 2 keV). Each channel consists of a charge-sensitive preamplifier, a shaper/gain stage, four-threshold discriminators (level-sensitive comparators), and four 18-bit counters. The four threshold levels are externally adjustable, which allows the user to define four energy bins between 5 keV and 60 keV. The ASIC chip readout is done by reading each channel-counter one after the other in a fixed sequence with an adjustable very fast peaking time (40 – 80 ns) and optimized for very low noise performance. More details of the Si strip detector and the associated ASIC can be found in a previous report (Hyo-Min Cho *et al.*, 2014).

A voltage of 70 V is placed across the silicon crystal of the detector to generate a bias electric field. As a photon interacts with the crystal and transfers energy above 3.6 eV to it at room temperature, an electron hole pair is created. Generated electrons are then collected at the back electrode and form a pulse whose height is proportional to the energy of the incoming photon. A count is registered if the pulse height was higher than the given threshold value. The lower boundaries of the energy bins are defined by four user-definable thresholds, therefore the count within an energy bin can be easily obtained by subtracting the count from its two adjacent thresholds. The detector can also be used in the spectrum collection mode where two thresholds can be simultaneously scanned over the whole energy range.

2.3. Simulation and Phantom preparation

A simulation study was conducted to investigate the performance of TFIR technique on our spectral breast CT system. First, a cylindrical phantom was designed with 10 cm in diameter

and 0.5 cm in length and filled with water. A 1.1 cm-diameter rod made of polyethylene, a 1.1 cm-diameter rod made of 8 mg/ml Iodine and a 0.61 cm-diameter rod made of B-100 bone-equivalent plastic were then inserted in this water phantom. Each rod was located 2.5 cm away from the phantom center and 90° to the next one. Such geometry was selected for the quantitative evaluation of MTF and CNR. Using the same geometry setting as that in the experiment, the simulation data were acquired with mean glandular dose (MGD) of 2.0 mGy and 6.0 mGy which were estimated from the previous simulation study (Boone, 1999). To validate the simulation with the experimental results, a small cylindrical phantom with 1.3 cm in diameter was also simulated. Three different concentrations of iodine (8, 16 and 32 mg/ml) were inserted into the PMMA background to provide different contrast levels (see figure 2a). CT images were generated with total entrance skin air kerma (ESAK) of 1.2, 2.4, and 3.6 mGy, which matches the experimental exposure conditions. In the experimental study, the same phantom was fabricated using a 1.3 cm PMMA cylinder to accommodate the finite length of the prototype detector (see figure 2b). The PMMA phantom material was chosen due to its similarity in x-ray attenuation to breast tissue (0.2074 cm^2/g for PMMA and 0. 2186 cm^2/g for breast tissue at 50 keV) (Hubbell and Seltzer, 1995).

2.4. Image acquisition, reconstruction and quantitative analysis

The phantom was placed on translation stage platform shown in figure 1. The rotation speed was approximately 0.976 rpm during image acquisition. The detector frame rate was set at 20 fps. Therefore, a total of 1229 frames were acquired for 360° rotation, which was derived from the mechanical design of the system. The tube potential and tube current were set at 65 kV and 0.6 mA, respectively, and the total ESAK without back scattering under the current setting was estimated to be 1.2 mGy for a full scan. The tube current was increased accordingly to deliver various radiation doses, 2.4 and 3.6 mGy. All data acquired with the silicon detector were corrected for non-uniformity across pixels, using a previously reported flat field correction technique (Le *et al.*, 2010). The flat field correction was made using an open source image processing software package (Sheffield, 2007). Images at various radiation doses were reconstructed by a conventional FBP technique with the software package from University of Michigan (Fessler) and the TFIR technique.

The spatial resolution and CNR for the FBP and TFIR techniques were compared in this study. For the spatial resolution comparison, the edge spread functions were extracted for different iodine concentrations from the images reconstructed by FBP at a full dose and by TFIR at the one-third dose. The task-based MTF was then calculated using the technique in the previous study (Boone and Seibert, 1994). For the CNR comparison, two region of interests (ROIs) were selected from the pure contrast and the pure background to calculate the average mean gray value and the standard deviation. The CNR was then calculated by:

$$CNR=\frac{M_C-M_B}{\sqrt{\sigma_C^2+\sigma_B^2}} \quad (4)$$

where M_i and σ_i are the average mean gray value and the standard deviation of the contrast target (C) and the background (B) from the selected ROIs, respectively.

3. Results

The task-based MTFs from our simulation study indicated that the spatial resolution remained intact for either different contrast targets or various radiation doses if the image was reconstructed by FBP, while it varied for the image reconstructed by TFIR. This was consistent to the results in recent studies (Richard *et al.*, 2012; Wilson *et al.*, 2013). In addition, it was also found that the spatial resolution was better for high contrast target (B-100 bone-equivalent plastic) and was similar for low contrast targets (8 mg/ml Iodine and Polyethylene) in the image reconstructed by TFIR with one-third of the radiation dose, 2.0 mGy, in comparison to the image reconstructed by FBP with the full radiation dose, 6.0 mGy (see figure 3).

In addition to the simulated results above, the experimental task-based MTFs were also calculated and shown in figure 4. It was indicated that the spatial resolution was independent of contrast targets for the images reconstructed by FBP, while it was target-dependent for TFIR (see figure 4a). The spatial resolution limit (MTF = 0.1) for the different contrast targets (8, 16, 32 mg/ml Iodine) were also compared between FBP with 3.6 mGy and TFIR with 1.2 mGy in simulation and experiment studies (see figure 4b) to quantitatively evaluate these two techniques. Both the simulation and the experimental results showed that TFIR with 1.2 mGy could achieve similar spatial resolution for the low contrast target and better spatial resolution for the high contrast target as compared to FBP with 3.6 mGy. It was also interesting that the spatial resolution was better for the TFIR with 1.2 mGy than that for an alternate TFIR with equivalent 1.2 mGy by using only one-third the projections by down-sampling from a 3.6 mGy sinogram. The simulated images produced a better spatial resolution than the experimental results for both FBP and TFIR methods. This overall improvement can be attributed to the increased noise level from the imperfect detector response function, which is not accounted in the simulation. Moreover, in comparison to the corresponding results from FBP, TFIR method performed slightly better in simulation than in experiment. This can be explained by the fact that TFIR requires detailed knowledge about the reconstruction geometry, which can be easily obtained in the simulation. In the experimental study, the geometric reconstruction parameters were derived from the system design and the detector specifications. Errors in the estimation of the imaging geometry may lead to a reduction in image quality during the reconstruction process.

For CNR comparison, the images were initially reconstructed by TFIR and FBP at various radiation doses (1.2, 2.4, and 3.6 mGy). The CNR was then calculated by selecting the ROIs in contrast targets and the background. An example of the reconstructed CT images from the experimental study is shown in figure 5. Significant CNR improvement can be found when comparing TFIR to FBP at the same exposure level. The quantitative analysis of CNR as a function of the exposure levels is shown in figure 6 for the simulation and experimental studies. The results show that the CNR from TFIR with 1.2 mGy is significantly better than FBP with 3.6 mGy in both the simulated and the experimental results. For example, in figure 6b, the CNR of TFIR with 1.2 mGy was 3.9 from the experimental study, approximately a factor of 1.7 higher as compared to CNR of 2.3 from FBP with 3.6 mGy. Different from the spatial resolution comparison, TFIR with 1.2 mGy and the alternate TFIR with an equivalent dose of 1.2 mGy (one-third projections of 3.6 mGy sinogram) had similar CNR values.

Similar results were observed in the large phantom from simulation, where the improvement of CNR between TFIR at MGD of 2 mGy and FPB at MGD of 6 mGy were found to be approximately 2.8 times for polyethylene, Iodine, and bone-equivalent plastic. The experimental and simulated improvements in the large phantom are expected to be similar given the good agreement between the simulation and experimental results from the small phantom shown in figure 6.

4. Discussions

In this study, the task-based MTF was calculated for the spatial resolution comparison. In the simulation, B-100 bone-equivalent plastic was used for high contrast target, while in the experiment 32 mg/ml iodine was selected. The reason for this change is because the experimental data is acquired with a small phantom, 1.3 cm in diameter, and the beam hardening will cause artifacts to other contrast target such as edge distortion if high contrast such as bone is used. 32 mg/ml Iodine is a contrast high enough in this study and the experimental result has proved this.

The task-based MTF was derived by extracting the edge spread function for each contrast target. It is initially expected to study MTF's dependence on the radiation dose for FBP with the experimental data. However, due to the high noise in images reconstructed by FBP, it is difficult to fit the edge spread function extracted from 8 mg/ml iodine, and even for 3.6 mGy dose the error is already high (see figure 4a). Therefore, it is not valuable to fit the edge spread function for the FBP images at lower dose such as 1.2 mGy. As a check, a larger dose of 6.0 mGy was delivered to the phantom and its task-based MTF was similar to that at 3.6 mGy dose.

Another interesting point in this study is that the spatial resolution is better for TFIR with the one-third dose compared to TFIR with the one-third projections (equivalent to the one-third dose in principle), while the CNR is almost the same. The possible explanation is that the more projections are acquired, the more accurate geometry information is achieved, which results in a better spatial resolution; the CNR is based on the average gray value from a large ROI and may not be affected in the same way. The results of this study suggest that it is better to lower the exposure per projection rather than lowering the number of projections to reduce the radiation dose. However, it should be also noted that each projection is noisier for more projections with low exposure compared to less projections with high exposure, which may be an issue for TFIR technique when the sinogram becomes too noisy for the image reconstruction. The limit of such approach is hard to predict, and therefore remains an open discussion.

It is noticed that images from TFIR with 1.2 mGy have almost double the CNR value compared to images from FBP with 3.6 mGy. Therefore, if only considering the CNR, the dose can be reduced further for TFIR. However, the spatial resolution will suffer because it becomes worse as the radiation dose reduces for the IR technique. Future studies to adopt the spatial resolution from FBP images and the CNR from TFIR images should be investigated. This hybrid technique should reduce the dose further, but it is beyond the scope of this study.

The iterative reconstruction technique usually needs a longer image processing time compared to FBP technique. However, the processing time of iterative reconstruction technique can be reduced significantly with a graphics processing unit (GPU) based system. In this study, TFIR is running in a desktop computer with a 2.5 GHz Intel Xeon CPU, 4 G RAM and NVidia GTX 680 video card. Reading the same sinogram, TFIR required approximately 10 seconds to reconstruct a single-slice CT image, while FBP required approximately 4 seconds without the GPU functionality. Therefore, GPU-based TFIR technique is now potentially feasible for fast clinical imaging tasks, particularly for spectral CT with material decomposition (Gao *et al.*, 2011), which will be experimentally investigated in our future work.

A future multi-slit multi-slice (MSMS) spiral CT system is proposed for breast CT. The implementation of this TFIR technique can result in a two-third dose reduction without losing the image quality compared to FBP technique. For a specific task with the MSMS spiral CT system such as detecting micro-calcification in the breast, it requires a high-resolution detector in addition to the necessary radiation dose. Since the high-resolution photon-counting detector has been available, the challenge remains on the reasonable radiation dose delivered to the objects. Considering the micro-calcification is a high contrast target compared to the normal breast tissue, this TFIR technique can further reduce the radiation dose compared to FBP technique to achieve a similar spatial resolution for this specific task. It should also be noted that current TFIR technique does not utilize the spectral information available from the energy-resolved photon-counting detector. Therefore, in theory, the observed dose reduction offered by the reconstruction technique should also be valid for a conventional charge-integrating detector with similar pixel pitch. However, future reconstruction algorithms which include the spectral information as prior constraint may lead to further dose reduction for the spectral CT system based on a photon-counting detector (Gao *et al.*, 2011).

5. Conclusion

This study demonstrates that the TFIR technique can significantly reduce the radiation dose by a factor of two-third for a CT reconstruction compared to FBP technique while achieving a better CNR and maintaining the same spatial resolution. The reconstruction time is about 10 seconds for a single-slice with a GPU system. Therefore, this TFIR technique can be potentially used in a future MSMS spiral CT system.

Acknowledgments

This work was supported in part by NIH/NCI grant R01CA13687. The authors would like to thank William Barber from DxRay Inc. for his technical support and fruitful discussions.

References

Anderson A, Kak A. Simultaneous algebraic reconstruction technique (SART): a superior implementation of the ART algorithm. Ultrasonic Imaging. 1984; 6:81–94. [PubMed: 6548059]

Barber, WC.; Nygard, E.; Wessel, JC.; Malakhov, N.; Wawrzyniak, G.; Hartsough, NE.; Gandhi, T.; Beck, TJ.; Taguchi, K.; Iwanczyk, JS. Large area photon counting X-ray imaging arrays for clinical

dual-energy applications. 2009 IEEE Nuclear Science Symposium and Medical Imaging Conference (NSS/MIC 2009); Florida, USA. 2009. p. 3029-31.

Bert C, Niederlohner D, Giersch J, Pfeiffer KF, Anton G. Computed tomography using the Medipix1 chip. Nuclear Instruments & Methods in Physics Research Section a-Accelerators Spectrometers Detectors and Associated Equipment. 2003; 509:240–50.

Beuville E, Cahn R, Cederstrom B, Danielsson M, Hall A, Hasegawa B, Luo L, Lundqvist M, Nygren D, Oltman E, Walton J. High resolution X-ray imaging using a silicon strip detector. Ieee Transactions on Nuclear Science. 1998; 45:3059–63.

Bian J, Han X, Yang K, Sidky E, Boone J, Pan X. A Preliminary Investigation of Reduced-view Image Reconstruction from Low-dose Breast CT Data. Proceedings of the SPIE-Physics of Medical Imaging. 2012; 8313:831325.

Bisogni MG, Del Guerra A, Lanconelli N, Lauria A, Mettivier G, Montesi MC, Panetta D, Pani R, Quattrocchi MG, Randaccio P, Rosso V, Russo P. Experimental study of beam hardening artifacts in photon counting breast computed tomography. Nuclear Instruments & Methods in Physics Research Section a-Accelerators Spectrometers Detectors and Associated Equipment. 2007; 581:94–8.

Boone JM. Glandular breast dose for monoenergetic and high-energy X-ray beams: Monte Carlo assessment. Radiology. 1999; 213:23–37. [PubMed: 10540637]

Boone JM, Seibert JA. An analytical edge spread function model for computer fitting and subsequent calculation of the LSF and MTF. Med Phys. 1994; 21:1541–45. [PubMed: 7869985]

Bornefalk H, Danielsson M. Photon-counting spectral computed tomography using silicon strip detectors: a feasibility study. Physics in Medicine and Biology. 2010; 55:1999–2022. [PubMed: 20299720]

Casteele E, Parizel P, Sijbers J. Quantitative evaluation of ASiR image quality: An adaptive statistical iterative reconstruction technique. Proceedings of the SPIE - Physics of Medical Imaging. 2012; 8313:83133F.

Chmeissani M, Frojdh C, Gal O, Llopart X, Ludwig J, Maiorino M, Manach E, Mettivier G, Montesi MC, Ponchut C, Russo P, Tlustos L, Zwerger A. First experimental tests with a CdTe photon counting pixel detector hybridized with a Medipix2 readout chip. IEEE Transactions on Nuclear Sciences. 2004; 51:2379–85.

Donoho DL. Compressed sensing. IEEE Transactions on Information Theory. 2006; 52:1289–306.

Elbakri IA, Fessler JA. Statistical image reconstruction for polyenergetic X-ray computed tomography. IEEE Trans Med Imaging. 2002; 21:89–99. [PubMed: 11929108]

Fessler, J. http://web.eecs.umich.edu/~fessler/irt/irt/

Frallicciardi PM, Jakubek J, Vavrik D, Dammer J. Comparison of single-photon counting and charge-integrating detectors for X-ray high-resolution imaging of small biological objects. Nuclear Instruments & Methods in Physics Research Section a-Accelerators Spectrometers Detectors and Associated Equipment. 2009; 607:221–2.

Gao H. Fast parallel algorithms for the x-ray transform and its adjoint. Med Phys. 2012; 39:7110–20. [PubMed: 23127102]

Gao H, Li R, Lin Y, Xing L. 4D conebeam CT via spatiotemporal tensor framelet. Med Phys. 2012; 39:6943–6. [PubMed: 23127087]

Gao H, Qi XS, Gao Y, Low DA. Megavoltage CT imaging quality improvement on TomoTherapy via tensor framelet. Med Phys. 2013; 40:081919. [PubMed: 23927333]

Gao H, Yu H, Osher S, Wang G. Multi-energy CT based on a prior rank, intensity and sparsity model (PRISM). Inverse Problems. 2011; 27:115012. [PubMed: 22223929]

Goldstein T, Osher S. The Split Bregman Method for L1-Regularized Problems. SIAM J Imaging Sci. 2009; 2:323–43.

Gordon R, Bender R, Herman G. Algebraic Reconstruction Techniques (ART) for Three-dimensional Electron Microscopy and X-ray Photography. Journal of Theoretical Biology. 1970; 29:471–6. [PubMed: 5492997]

Herman, GT. Image Reconstruction from Projections: Fundamentals of Computerized Tomography. Academic Press; New York: 1980.

Hernandez D, Michel E, Kim HS, Kim JG, Han BH, Cho MH, Lee SY. Iterative image reconstruction in spectral-CT. Proceedings of the SPIE-Physics of Medical Imaging. 2012; 8313:831330.

Hubbell JH, Seltzer SM. Tables of x-ray mass attenuation coeeficient and mass energy absorption coefficients 1 keV to 20 MeV for elements Z=1 to 92 and 48 additional substances of dosimetric interest. 1995 NIST Report No. NISTIR 5632.

Cho, Hyo-Min; Barber, William C.; Ding, Huanjun; Iwanczyk, Jan S.; Molloi, Sabee. Characteristic performance evaluation of a photon counting Si strip detector for low dose spectral breast CT imaging. Med Phys. 2014 to be published.

Jorge, N.; Stephen, JW. Numerical optimization. New York, NY: Springer; 1999.

Kak, AC.; Slaney, M. Principles of Computerized Tomographic Imaging. IEEE Press; New York: 1988.

Le HQ, Ducote JL, Molloi S. Radiation dose reduction using a CdZnTe-based computed tomography system: Comparison to flat-panel detectors. Med Phys. 2010; 37:1225–36. [PubMed: 20384260]

Makeeva A, Dasb M, Glicka SJ. Investigation of statistical iterative reconstruction for dedicated breast CT. Proceedings of the SPIE-Physics of Medical Imaging. 2012; 8313:83131W.

Pachon J, Yadava G, Pal D, Hsieh J. Image Quality Evaluation of Iterative CT Reconstruction Algorithms: A Perspective from Spatial Domain Noise Texture Measures. Proceedings of the SPIE-Physics of Medical Imaging. 2012; 8313:83132K.

Richard S, Husarik DB, Yadava G, Murphy SN, Samei E. Towards task-based assessment of CT performance: System and object MTF across different reconstruction algorithms. Med Phys. 2012; 39:4115. [PubMed: 22830744]

Sheffield JB. Image J, a useful tool for biological image processing and analysis. Microscopy and Microanalysis. 2007; 13:200–1.

Shikhaliev PM. Computed tomography with energy-resolved detection: a feasibility study. Physics in Medicine and Biology. 2008; 53:1475–95. [PubMed: 18296774]

Shikhaliev PM, Fritz SG. Photon counting spectral CT versus conventional CT: comparative evaluation for breast imaging application. Physics in Medicine and Biology. 2011; 56:1905–30. [PubMed: 21364268]

Sidky E, Kao C, Pan X. Accurate image reconstruction from few-views and limited-angle data in divergent-beam CT. Journal of XRay Science and Technology. 2006; 14:119–39.

Taguchi, K.; Srivastava, S.; Kudo, H.; Barber, WC. Enabling photon counting clinical X-ray CT. 2009 IEEE Nuclear Science Symposium and Medical Imaging Conference (NSS/MIC 2009); 2009.

Wang X, Meier D, Oya P, Maehlum GE, Wagenaar DJ, Tsui BMW, Patt BE, Frey EC. Microcomputed Tomography with A Second Generation Photon-counting X-ray Detector-Contrast Analysis and Material Separation. Proceedings of the SPIE-The International Society for Optical Engineering. 2010; 76221B:8.

Wilson JM, Christianson OI, Richard S, Samei E. A methodology for image quality evaluation of advanced CT systems. Med Phys. 2013; 40:031908. [PubMed: 23464323]

Xu Q, Yu H, Mou X, Zhang L, Jiang H, Wang G. Low-dose x-ray CT reconstruction via Dictionary learning. IEEE Trans Med Imaging. 2012; 31:1682–97. [PubMed: 22542666]

Yu HY, Wang G. Compressed sensing based interior tomography. Physics in Medicine and Biology. 2009; 54:2791–805. [PubMed: 19369711]

Zhao B, Ding H, Lu Y, Wang G, Zhao J, Molloi S. Dual-Dictionary Learning-Based Iterative Image Reconstruction of Spectral Computed Tomography Application. Phys Med Biol. 2012; 57:8217–29. [PubMed: 23192234]

Zhao B, Gao H, Ding H, Molloi S. Tight-frame based iterative image reconstruction for spectral breast CT. Med Phys. 2013; 40:031905. [PubMed: 23464320]

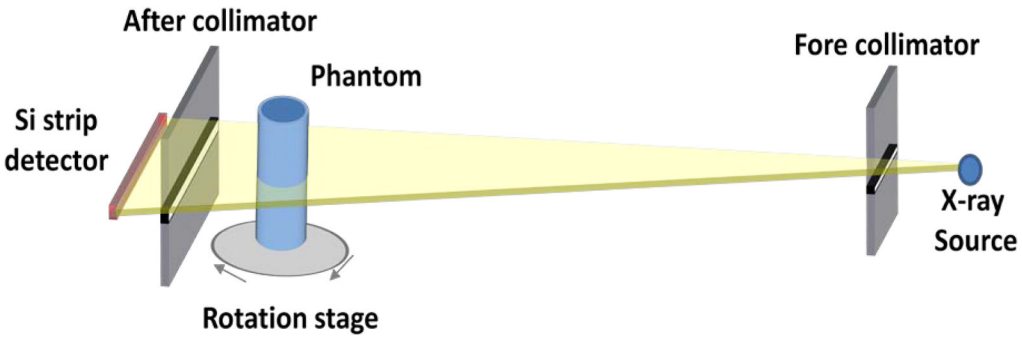

Figure 1.
Schematic drawing of the spectral CT system based on a Silicon strip photon-counting detector.

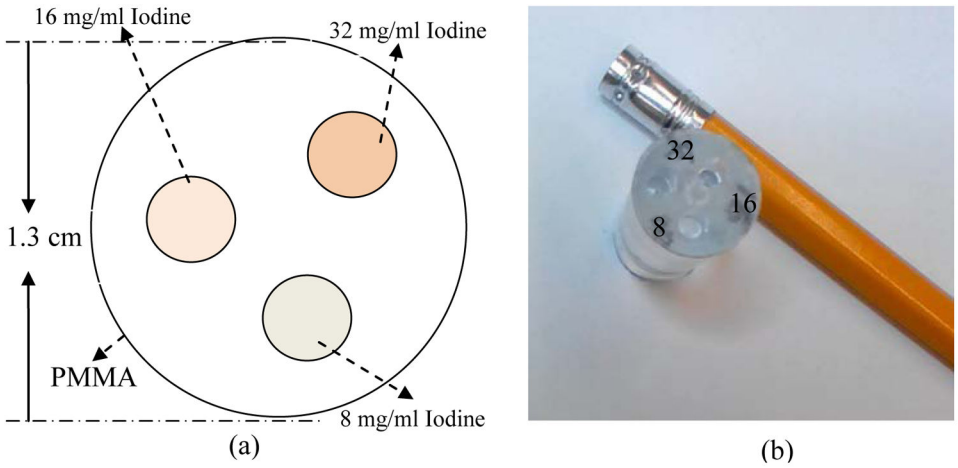

Figure 2.

(a) Layout and (b) a picture of a phantom with different Iodine concentrations are shown. The diameter is 0.3 cm for each contrast cell.

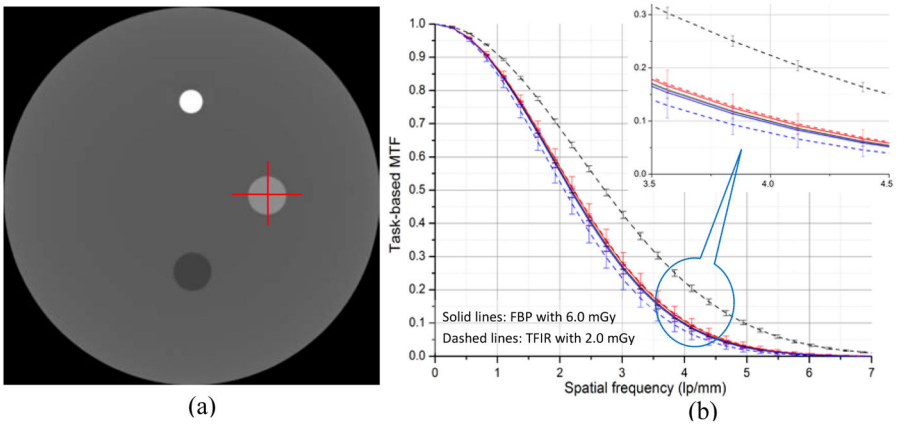

Figure 3.

(a) A CT image reconstructed by FBP with 6.0 mGy from the simulation; Red lines indicated the positions to extract the edge spread function. (b) Task-based MTF calculated from the FBP image with 6.0 mGy (solid lines) and from the TFIR image with 2.0 mGy (dashed lines) for different contrast targets (blue for Polyethylene, red for 8 mg/ml Iodine and black for B-100 bone-equivalent plastic).

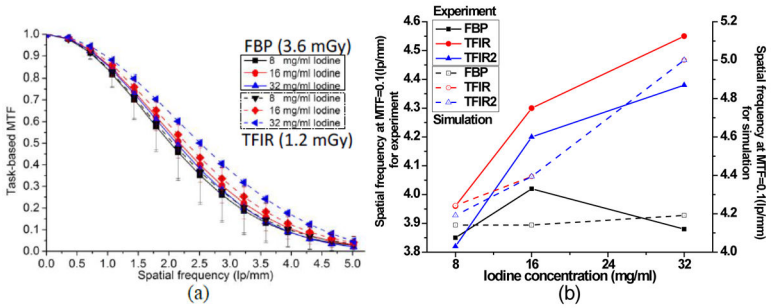

Figure 4.

(a) The experimental task-based MTF calculated from the FBP image with 3.6 mGy (solid lines) and from the TFIR image with 1.2 mGy (dashed lines) for different Iodine concentrations. (b) The resolution limit (MTF = 0.1) as a function of Iodine concentration for different reconstruction techniques studied in both simulation and experiment. The y-axis on the left and right side of the chart are special frequency for experiment and simulation, respectively.

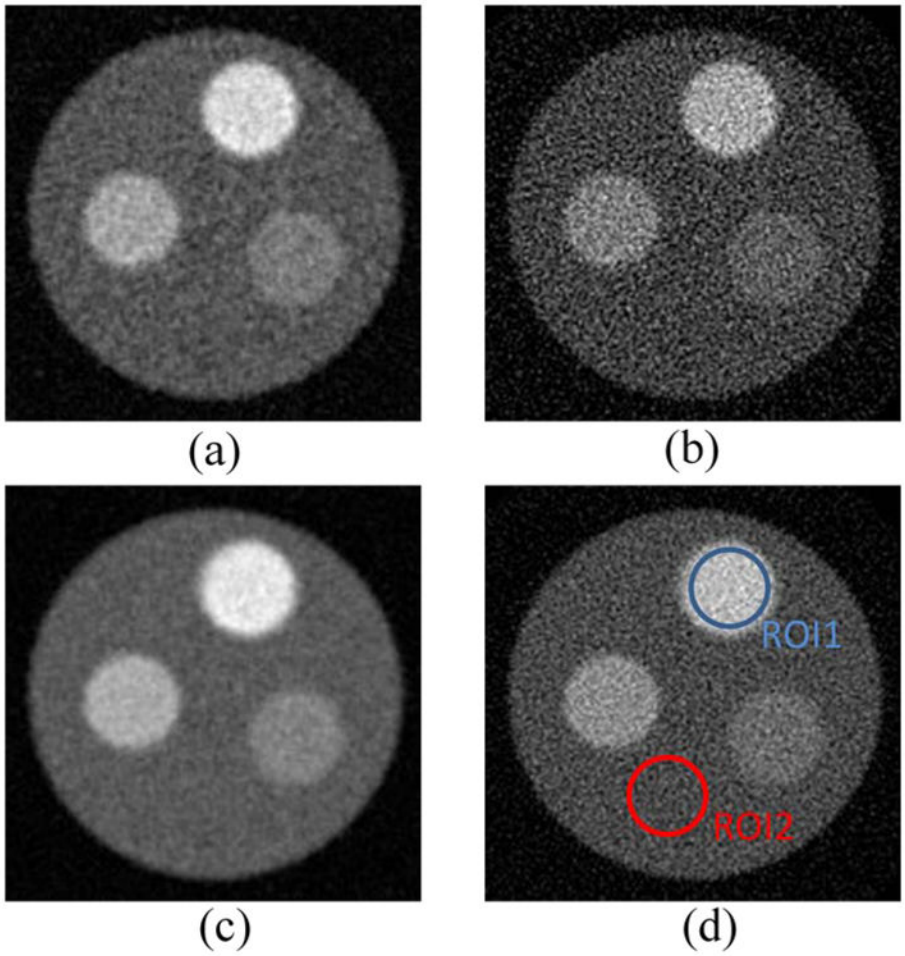

Figure 5.

The experimental CT image reconstructed from, (a) TFIR with 1.2 mGy, (b) FBP with 1.2 mGy, (c) TFIR with 3.6 mGy and (d) FBP with 3.6 mGy. Two circles indicate the ROIs selected from contrasts (ROI1) and from background (ROI2) to calculate the CNR. All images were shown with the same window and level.

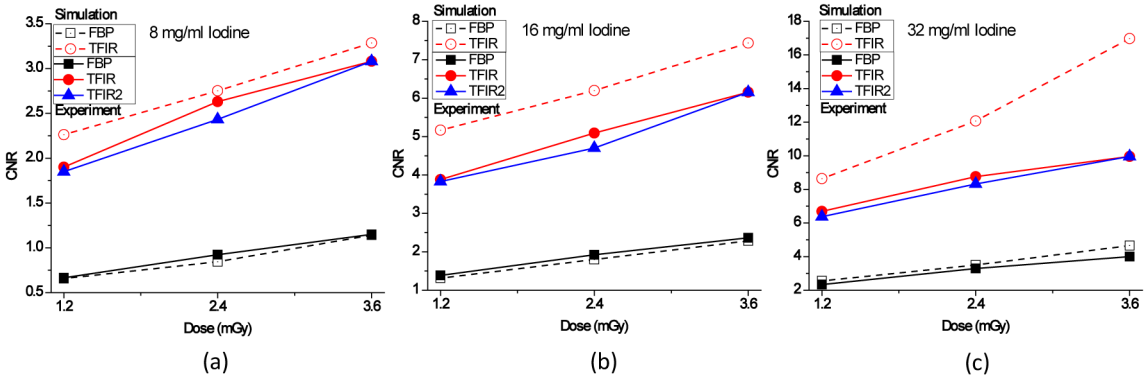

Figure 6.

The simulated (dashed lines) and experimental (solid lines) measurement of CNR as a function of exposure level for different Iodine concentrations, (a) 8 mg/ml, (b) 16 mg/ml and (c) 32 mg/ml with different reconstruction techniques (TFIR2 was down-sampled projections from 3.6 mGy sinogram).